

Toward Data-Assisted Particle-Fluid Simulations of Heat Transfer in Blast Furnaces

Thomas Lichtenegger* and Stefan Pirker

Detailed particle-fluid simulations of moving bed reactors such as blast furnaces (BFs) are computationally very expensive. The wide range of temporal scales from short-lived micromechanics to slow, macroscopic transport makes it almost impossible to study e.g., heat transfer over process-relevant time scales. However, a recently introduced approach that uses high-fidelity data obtained with the discrete element method (DEM) enables extremely fast data-assisted simulations. Using this methodology, calculations are conducted, which are efficient enough to study granular motion through a BF slot model subject to heat transfer between the hot blast and the solid phase over many hours. These long durations make it possible to determine the thermal steady state including shape and location of the cohesive zone (CZ). While other approaches either have to predefine its properties or are bound to very small domain sizes, this novel strategy is applied to a large-scale BF slot model with about 28 m height and 15 m width with hardly any prior knowledge. It constitutes an important step toward virtual experiments on BFs under realistic conditions and will allow researchers to gain new insights, perform variations of operating parameters, and ultimately build an online monitoring system.

time scales has prevented a detailed, fully resolved description of real-scale BFs so far, because the huge number of coke and ore grains exceeds the capabilities of current computational methods by orders of magnitude. Similarly, the contact mechanics of stiff materials^[1] requires very small time steps, whereas relevant process durations encompass several hours (or even more), which is such a massive scale separation that it goes far beyond current computational resources. These discouraging obstacles are countered by the significant benefits of carrying out numerical in addition to on-plant experiments: The former are much safer, cheaper, and more flexible, and they provide much more information which might be inaccessible from the latter (e.g., on the conditions in the center of the BF hearth).

Due to the limited computational resources, first attempts to simulate moving bed reactors used a fully Eulerian approach, i.e., the granular material was

described with continuous fields for velocity and packing fraction just as the interstitial gas. Subsequently, this approach was extended with other phases such as liquid iron and slag or dust^[2] and more physics such as heat and mass transfer or thermochemical reactions.^[3–6]

Although numerically not too expensive, such Eulerian methods generally suffer from the lack of particle-based representation. As the contact mechanics of densely packed, solid grains is very complicated, a description in terms of field quantities such as the local amount of particle mass and momentum is connected to a significant uncertainty in the resulting meso- and macroscopic flow patterns, which also affects transport of heat and hence the gas dynamics. Furthermore, a description based on discrete particles allows for a straightforward study of sophisticated inner-grain processes such as chemical conversion of hematite to magnetite, wüstite, and finally to iron.^[7]


The discrete element method (DEM) introduced by Cundall and Strack^[8] combined with computational fluid dynamics (CFD–DEM)^[9,10] constitutes the method of choice to simulate dense particulate flows. It tracks each grain, calculates the forces from the surrounding particles and fluid phase, and hence obtains relatively accurate trajectories. However, high numerical costs limit this approach usually to $O(10^6)$ elements. Even though combining several particles into one parcel with modified material properties^[11,12] (e.g., shear modulus or coefficient of friction) allows to carry out larger-scale simulations, most investigations

1. Introduction

The study of moving bed reactors in general and blast furnaces (BFs) in particular has attracted a large number of researchers from various disciplines. In addition to their undisputable relevance for worldwide steel production and related industries, these systems constitute a substantial challenge for scientists interested in numerical simulations of granular matter and particle–fluid interactions. The extreme variety of length and

Dr. T. Lichtenegger, Prof. S. Pirker
Department of Particulate Flow Modelling
Johannes Kepler University
4040 Linz, Austria
E-mail: thomas.lichtenegger@jku.at

Dr. T. Lichtenegger, Prof. S. Pirker
Linz Institute of Technology (LIT)
Johannes Kepler University
4040 Linz, Austria

 The ORCID identification number(s) for the author(s) of this article can be found under <https://doi.org/10.1002/srin.202000132>.

© 2020 The Authors. Published by WILEY-VCH Verlag GmbH & Co. KGaA, Weinheim. This is an open access article under the terms of the Creative Commons Attribution License, which permits use, distribution and reproduction in any medium, provided the original work is properly cited.

DOI: 10.1002/srin.202000132

of packed beds in general and BF's in particular with CFD–DEM have focused on specific phenomena. Although material charging,^[13] burden descent,^[14–16] raceway formation,^[17–21] heat transfer from a hot gas to the granular phase^[22] or within it,^[23,24] reduction of iron ore^[7] or the dynamics of liquid iron and slag through/around the deadman in the hearth^[25] have already been investigated separately, a combined, accurate model applicable to a BF including several^[26] or all of these processes is extremely difficult to create. In addition to practical challenges such as unavailability of various in-house codes or the lack of appropriate interfaces to couple them, the mentioned phenomena take place over time scales which are all far beyond the scope of DEM if applied to such large reactor sizes that, e.g., both charging at the top and liquid tapping close to the bottom can be considered. Unless slow subprocesses are artificially sped up, e.g., with a scaling approach,^[27] a massive spread of temporal scales remains to be closed.

Over the last decade, first attempts to tackle this problem using data-assisted approaches with precalculated aspects of the granular dynamics were made. Although similar ideas are well-known in the CFD community (e.g., flamelet libraries^[28]), only a few authors have applied them to dense, particulate flows with their complicated contact mechanics so far. Bluhm-Drenhaus et al.^[29] and Krause et al.^[30,31] described a two-stage technique where they first obtained particle positions and velocities from pure DEM and then used the resulting trajectories for coupled CFD simulations including heat and mass transfer of lime shaft kilns over several hours. Arguing along similar lines, Bednarek et al.^[32] time-extrapolated grain paths to study mixing of different grain species over long durations at little computational costs. In contrast to such Lagrangian, position-based methods, Vångö et al.^[33] used a database of particle volume fraction fields corresponding to different liquid levels in a BF hearth from CFD–DEM to accelerate subsequent simulations of the drainage process. Instead of calculating the position of the deadman from the dynamics of each single grain depending on the remaining liquid iron and slag, they looked it up in the database so that they only had to solve the fluid problem. Similarly, Lichtenegger^[34] used short-term CFD–DEM simulations to obtain the granular velocity and volume fraction fields and replaced solid particles with noninteracting tracers in the next step. These simply followed the prescribed field lines while the gas dynamics was calculated according to the current bed conditions such as location of coke and ore layers or the local temperature. In contrast to the Lagrangian methods of Bluhm-Drenhaus et al.,^[29] Krause et al.,^[30,31] and Bednarek et al.,^[32] which provide more details on the single-particle level, this approach is simpler concerning information requirements because only one field for velocity and one for packing density needs to be obtained and stored. Hence, it could easily be embedded into the more general framework of Eulerian recurrence CFD^[35] and can in principle handle both pseudo-steady and recurrent dynamics because it allows for very efficient combination, extrapolation and/or updates of flow information. As a matter of fact, the pseudo-steady problem of Lichtenegger^[34] can be regarded as a special case of recurrent motion for which the method has been used repeatedly. However, the dense packing of granular beds and the strong thermal gradients in BF's required specific handling.

Compared to CFD–DEM, this approach was so fast that the temperature evolution in a BF could be studied over the course of 24 h process time, which was sufficient to reach the thermal steady state starting from a cold, initial guess. As all information about the granular dynamics was retrieved from a short-term CFD–DEM simulation, gradual changes in the trajectories over long durations could not be captured. Consequently, the shape of the raceways or the location of the cohesive zone (CZ) had to be predefined and did not change during the long-term, data-assisted simulation. Although the former can be obtained from a CFD–DEM calculation, the latter is determined by the temperature distribution which can only be found from a long-term study. However, it is well known that the position of the CZ has a significant influence on the resulting flow patterns.^[16] In this work, we combine fast, data-assisted simulations to achieve a thermal steady state with intermittent CFD–DEM simulations to update the location of the CZ and its influence on the particle flow fields. This way, we can include gradual changes in the particle dynamics due to shifting of the softening and melting zones. Finally, we find the thermal steady state with its corresponding CZ.

2. Methodology

2.1. Equations of Motion of Particulate Flows

2.1.1. Particle Equations

Solid particles are characterized by their position, velocity (both translational and rotational), mass, size, and any inner properties such as temperature or chemical composition. Their trajectories can be obtained from Newton's second law

$$\dot{\mathbf{r}}_i = \mathbf{v}_i \quad (1)$$

$$m_i \dot{\mathbf{v}}_i = \mathbf{F}_i^{(p-p)} + \mathbf{F}_i^{(p-f)} + \mathbf{F}_i^{(ext)} \quad (2)$$

where $\mathbf{F}_i^{(p-p)}$ is the particle–particle interaction mainly due to contacts, $\mathbf{F}_i^{(p-f)}$ represents the forcing due to the surrounding fluid and $\mathbf{F}_i^{(ext)}$ comprises forces of external origin such as gravity. The particle–particle interaction is often approximated as a pairwise sum

$$\mathbf{F}_i^{(p-p)} = \sum_{j \neq i} (\mathbf{F}_{ij}^{(n)} + \mathbf{F}_{ij}^{(t)}) \quad (3)$$

of spring–dashpot models for spherical grains, that depend on the normal and tangential overlap of particles in contact.^[1,8] In many cases, the most important contributions to the particle–fluid interaction are pressure gradients and the drag force, i.e., the resistance to relative velocity between solid and fluid phase (see Section 2.1.2). In addition to Equation (1) and (2), their counterparts for angular orientation and velocity need to be solved, but are not explicitly spelled out here.

For large-scale simulations, it has become common practice to replace n^3 particles of diameter d with a single parcel with diameter nd , which is referred to as coarse-graining. Such a procedure implies an adaption of DEM material parameters either based on closure rules^[11,12] or on small-scale calibration simulations of e.g., the angle of repose. For the particle–fluid interaction, one

has to keep in mind that each parcel represents several actual grains, hence it needs to be evaluated in terms of d and finally scaled with n^3 . Clearly, this approach is increasingly challenged with growing parcel size and breaks down once it gets close to the geometric dimensions of a problem.

Similar as momentum in Equation (2), the temperature of a grain with mass m_i and specific heat capacity C_p not only changes to due heat exchange with surrounding particles and fluid but also due to inner sinks or sources, e.g., because of chemical reactions, viz

$$m_i C_p \dot{T}_i = \dot{Q}^{(p-f)}(T_i - T_f(\mathbf{r}_i)) + \sum_{i \neq j} \dot{Q}^{(p-p;cond)}(T_i - T_j) + \sum_{i \neq j} \dot{Q}^{(p-p;rad)}(T_i^4 - T_j^4) + \dot{Q}^{(chem)} \quad (4)$$

Among the various correlations available for particle–fluid heat transfer, we used that of Ranz and Marshall.^[36] Note that in BF's and similar reactors, the convective heat transfer coefficient is often massively overestimated and needs to be scaled down, which might be caused by flow irregularities and channel formation^[37] but is currently an open question. For the present work, we reduced it by a factor of 10.

The interparticle exchange of heat due to conduction, in contrast, can be calculated in a relatively straightforward fashion because it mainly depends of the contact area which is directly accessible in a DEM simulation from the particle positions and sizes. Although it is well-known that radiative heat transfer plays a dominant role at high temperatures, we did not include it in the present article to keep the current considerations as simple as possible. Nevertheless, we point out that approximate models for this computationally rather complex transfer mechanism exist, which are applicable for large-scale investigations.^[24,31]

Temperature can clearly affect other particle properties, especially close to the melting point. Concerning the focus of this work, we want to study the gradual softening and finally melting of ore grains on their way through the CZ. To this end, we assume that a particle starts shrinking if its temperature is above a certain lower threshold T_{soft} . At the same time, its mass needs to be conserved so that we introduce a pseudo-volume factor f_{eff} such that

$$\frac{4\pi}{3} r^3 \rho f_{eff} = m \quad (5)$$

As monodisperse spheres have a maximum random packing fraction of about $\alpha_{max} = 0.64$,^[38] the pseudo-volume factor is limited by $1 \leq f_{eff} \leq 1/\alpha_{max}$, where the upper bound corresponds to complete deformation so that the whole available volume can be occupied. Hence, we suggest

$$f_{eff} = 1 + \frac{T - T_{soft}}{T_{melt} - T_{soft}} \left(\frac{1}{\alpha_{max}} - 1 \right) \quad (6)$$

if $T_{soft} < T < T_{melt}$. Keeping the mass of each particle fixed, its effective radius shrinks with increasing temperature so that more grains fit inside a given volume and their packing fraction grows. Once a particle has reached T_{melt} , it is removed from the simulation because “it has melted and trickled down” through the solid coke bed.

2.1.2. Fluid Equations

If particles occupy a fraction $\alpha_p(\mathbf{r}, t)$ of the local volume, only $\alpha_f(\mathbf{r}, t) = 1 - \alpha_p(\mathbf{r}, t)$ remains for the fluid phase. As a consequence, the Navier–Stokes equations for a fluid with density $\rho_f(\mathbf{r}, t)$ and velocity $\mathbf{u}_f(\mathbf{r}, t)$ take the form^[39]

$$\frac{\partial}{\partial t} \alpha_f \rho_f + \nabla \cdot \alpha_f \rho_f \mathbf{u}_f = 0 \quad (7)$$

$$\frac{\partial}{\partial t} \alpha_f \rho_f \mathbf{u}_f + \nabla \cdot \alpha_f \rho_f \mathbf{u}_f \mathbf{u}_f = \alpha_f \nabla \cdot \boldsymbol{\sigma}_f + \mathbf{f}^{(drag)} \quad (8)$$

where the stress tensor for a Newtonian fluid with viscosity μ_f is given by

$$\boldsymbol{\sigma}_f = -p\mathbf{I} + \mu_f(\nabla \mathbf{u}_f + (\nabla \mathbf{u}_f)^t) + \frac{2}{3} \mu_f \mathbf{I} \nabla \cdot \mathbf{u}_f \quad (9)$$

with the unit matrix \mathbf{I} , and $\mathbf{f}^{(drag)}$ is the drag force density closely related to the particle–fluid interaction

$$\mathbf{F}_i^{(p-f)} = -V_i \nabla p - \frac{V_i}{\alpha_p} \mathbf{f}^{(drag)}(\mathbf{r}_i) \quad (10)$$

As fluid density and pressure are connected via temperature, the energy transport equation

$$\begin{aligned} \frac{\partial}{\partial t} \alpha_f \rho_f (\epsilon_f + K_f) + \nabla \cdot \alpha_f \rho_f \mathbf{u}_f (\epsilon_f + K_f) \\ = -\nabla \cdot \alpha_f p_f \mathbf{u}_f + \nabla \cdot \alpha_f k_f^{(eff)} \nabla T_f + \dot{q}^{(p-f)} \end{aligned} \quad (11)$$

for internal and kinetic energy ϵ_f and $K_f = \mathbf{u}_f^2/2$ needs to be solved together with Equation (7) and (8). In addition to the work for compression against pressure and thermal conduction with effective conductivity $k_f^{(eff)}$,^[40] heat transferred between particulate and fluid phase with rate $\dot{q}^{(p-f)} = -\frac{\alpha_p}{V_p} \dot{Q}^{(p-f)}$ appears in the transport equation.

The CFD–DEM Equation (1), (2), (4), (7), (8), and (11) for compressible, nonisothermal conditions have been applied successfully to a variety of systems. We have validated our implementation against measurements on a gas–solid fluidized bed.^[35]

2.2. Simplified Equations of Motion under Pseudo-Steady Conditions

Even though granular dynamics is inherently not especially smooth (“stick–slip motion”) on a single- or few-grain level, it can become steady on meso- and macroscopic scales under appropriate conditions. In such cases, although the velocity of a single particle contains abrupt fluctuations, the granular velocity field $\mathbf{u}_p(\mathbf{r})$ is approximately time-independent. Once $\mathbf{u}_p(\mathbf{r})$ has been obtained, e.g., from a short-term CFD–DEM simulation, it may be used to calculate the future trajectories of each particle by moving it with small steps according to

$$d\mathbf{r}_i = dt \mathbf{u}_p(\mathbf{r}_i) + d\mathbf{r}_{md} \quad (12)$$

where $d\mathbf{r}_{md}$ approximates the influence of particle-contacts. Comparing the actual, local volume fraction with that obtained

from the previous CFD–DEM simulation, random fluctuations dr_{rnd} are imposed that grow with increasing deviation between the volume fractions. This way, no real contact detection or force calculation between neighboring grains is necessary, which tremendously reduces the computational costs of the approach and allows for much larger time steps. While they are limited by the Hertz collision time in DEM, they are now controlled by the much tamer spatial variation of the velocity field the curvature of which needs to be resolved with Equation (12). Only the fluid Equation (7), (8), and (11) and the particle temperature Equation (4) with an effective intergrain thermal conductivity^[41] need to be solved. The interested reader can find more information, in particular on the partly stochastic contribution, in an earlier publication.^[34]

As we replace solid grains with noninteracting tracers following the granular velocity field given by previously obtained data, we call this approach data-assisted CFD with tracers. It is of course restricted to cases where the granular motion is steady on mid and large scales, but fluid dynamics and thermal properties are treated with the same generality as in CFD–DEM and can show any type of transient behavior.

3. Simulation Setup

The code for our simulations was implemented in the framework of OpenFOAM, LIGGGHTS^[42] and CFDEMcoupling^[43] and may be obtained upon request from our repository <https://github.com/ParticulateFlow/>.

3.1. Work Flow of Coupled CFD–DEM and Data-Assisted CFD Simulations

While CFD–DEM can provide high-quality data for short time ranges, data-assisted CFD with tracers can cover much longer process durations but is restricted to a fixed particle velocity field. If the latter changes slowly over time because of some long-term process such as variations in the temperature field, both methods need to be combined as shown in **Figure 1**. First, a CFD–DEM run for $\tau_{\text{CFD-DEM}}$ is performed with an initial guess for the position of the CZ where ore particles first deform and then leave the simulation. The particle velocities and volumes are binned on a grid and time-averaged over a short window to obtain the granular velocity and volume fraction fields $\bar{u}_p(\mathbf{r})$ and $\bar{\alpha}_p(\mathbf{r})$. Furthermore, the positions $\{\mathbf{r}_i\}$ after $\tau_{\text{CFD-DEM}}$ need to be stored for the following data-assisted CFD run for which they serve as initial conditions. Then, over the course of $\tau_{\text{d.a.CFD}} \gg \tau_{\text{CFD-DEM}}$, tracer motion including heat exchange with the surrounding gas flow is calculated. From the particle temperature field $T_p(\mathbf{r}, \tau_{\text{d.a.CFD}})$, the new location of the CZ is obtained and communicated to the next CFD–DEM simulation, where over $\tau_{\text{CFD-DEM}}$ the corresponding, new $\bar{u}_p(\mathbf{r})$ and $\bar{\alpha}_p(\mathbf{r})$ are calculated. The final particle locations from the previous CFD–DEM need to be used as initial conditions because they cannot be provided by data-assisted CFD which due to the lack of particle contacts does not produce packings without overlaps. With the updated particle velocity and volume fraction fields, another data-assisted CFD run is started. Particle temperatures are initialized with the temperature field after the previous data-assisted simulation

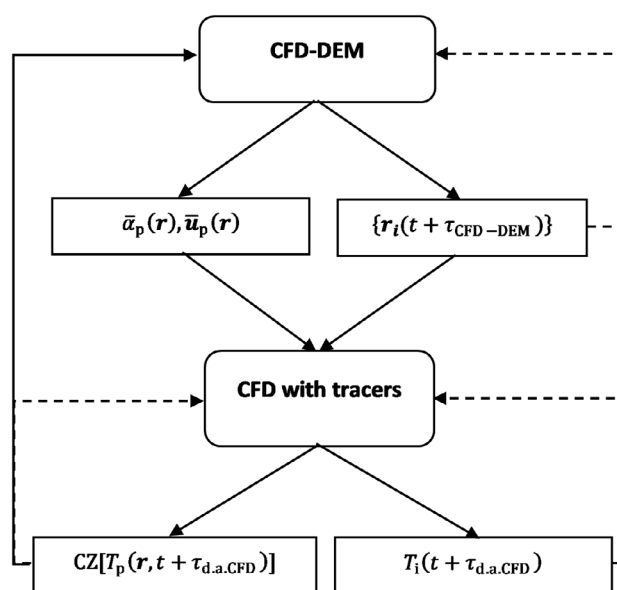


Figure 1. Work flow of coupled CFD–DEM and data-assisted CFD simulations. While CFD–DEM provides time-averaged particle velocity and volume fraction fields as well as grain positions, data-assisted CFD calculates the temperature distribution according to this information. The latter is then used to update the location of the CZ where grains are removed in both CFD–DEM and data-assisted CFD simulations. Thick, straight arrows represent the flow of information and the sequence of carried out calculations; dashed arrows indicate information which is also used by the next instance of the same type of simulation and not only by the immediately following one of the other kind.

$T_p(\mathbf{r}, \tau_{\text{d.a.CFD}})$ and are subject to further calculation from which a new CZ is obtained.

This alternation between detailed, numerically expensive CFD–DEM and approximate, fast data-assisted CFD can be repeated arbitrarily often until both the temperature field and the location of the CZ have converged. While $\tau_{\text{CFD-DEM}}$ needs to be sufficiently large such that the time-window-averaged particle velocity and volume fraction fields have converged after an update of the CZ, $\tau_{\text{d.a.CFD}}$ should allow for a substantial change in the temperature field.

3.2. Setup of the CFD–DEM and Data-Assisted CFD Simulations

In this work, we used a full-height slot model of a BF with about 28 m bed height and a width of up to 15 m. Its depth of 1.2 m corresponded to the distance between two tuyeres. Although such a slot model cannot picture the full physics of a 3D BF, it is still useful to develop novel computational methods at relatively low numerical costs before applying them to the 3D case.

Altogether, our simulation contained $N_p \approx 1.1 \times 10^5$ coarse-grained parcels. We chose species-dependent scaling factors such that all resulting parcels had approximately the same size and were small enough to resolve different material layers but did not lead to an excessive overall number of grains.

A sketch of the geometry can be seen in **Figure 2** together with the initial guess for the shape and location of the CZ. In the

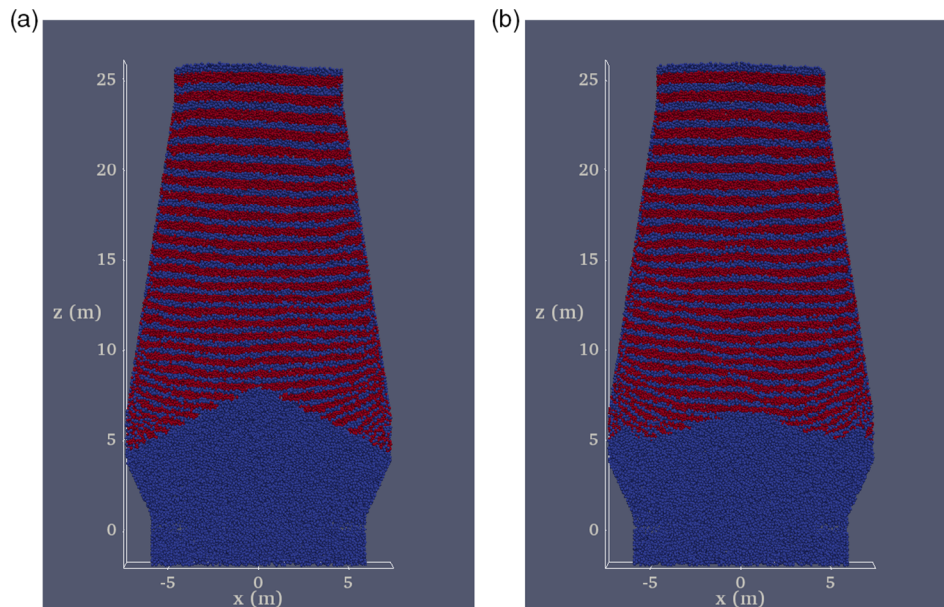


Figure 2. a) Initial and b) final particle configuration. Although the upper part of the BF was filled with layers of coke (blue) and ore (red), only coke was present in the region below the CZ. The shape and location of the CZ changed considerably from the initial guess of an inverted V toward a W.

CFD–DEM simulations, we removed coke grains with a predefined rate in the raceway regions and modified ore properties in the CZ according to Equation (6) before deleting them. To this end, we chose $T_{\text{soft}} = 1475 \text{ K}$ and $T_{\text{melt}} = 1675 \text{ K}$. The coke removal rate of $\dot{m}_{\text{coke}} = 500 \text{ kg s}^{-1}$ per raceway was artificially high to enable the passage of several layers within the scope of a CFD–DEM simulation. The obtained particle velocity field $\vec{u}_p(\mathbf{r})$ was corrected by rescaling it such that a realistic descent rate of $v_{\text{desc}} = 2 \text{ mm s}^{-1}$ at the furnace top was achieved. The most important particle properties such as diameter, density, or coarse-graining factors are listed in **Table 1**. The used thermal models are given in **Table 2**. More details, e.g., on DEM-specific parameters can be found in our earlier publication.^[34]

Table 1. Particle properties.

Property	Coke	Ore
d_p [m]	0.044	0.015
c_{cg}	4	10
ρ_p [kg m^{-3}]	800	3000
C_p [$\text{J kg}^{-1} \text{ K}^{-1}$]	850	600
k_p [$\text{W m}^{-1} \text{ K}^{-1}$]	1.7	80

Table 2. Thermal models.

Property	Model
Convective heat transfer	Ranz and Marshall ^[36]
Eff. thermal conductivity	Syamlal and Gidaspow ^[40]
Intergrain thermal conductivity	Carson et al. ^[41]
Equation of state	ideal gas

As we did not take any chemical reactions into consideration in this work, we assumed that the hot blast entered the furnace with a temperature of $T_{\text{in}} = 2600 \text{ K}$ at $\mathbf{u}_{\text{in}} = 200 \text{ m s}^{-1}$. Similar as Zhang et al.,^[44] we chose a fixed heat loss coefficient of $h_{\text{wall}} = 20 \text{ W m}^{-2} \text{ K}^{-1}$ over the walls with $T_{\text{wall}} = 293 \text{ K}$.

Time steps of $\Delta t_{\text{CFD}} = 2.5 \times 10^{-4} \text{ s}$ and $\Delta t_{\text{DEM}} = 2.5 \times 10^{-5} \text{ s}$ led to numerically stable conditions. Close inspection of the results showed that we could obtain the particle velocity and volume fraction fields with satisfying accuracy already with averaging windows of $t_{\text{ave}} = 10 \text{ s}$ and simulation durations $\tau_{\text{CFD-DEM}} = 20 \text{ s}$.

Without the need for contact detection and resolution, we could use comparatively large time steps $\Delta t_{\text{tracer}} = 0.25 \text{ s}$ four orders of magnitude larger than those for DEM in the data-assisted simulations. Furthermore, since gas-phase properties changed much more rapidly than those of the solid grains, we assumed that the former adapted to the latter instantaneously so that we solved the time-independent versions of Equation (7), (8), and (11) for each tracer time step. This allowed us to carry out multiple episodes of 5 h process time each. Other properties such as material parameters were the same in both cases.

4. Results and Discussion

The initial particle configuration for our coupled simulations can be seen in Figure 2a. We created it by first filling the whole furnace with coke and then removing it gradually in the raceway regions. Once the top material level had fallen below 26.1 m, a pair of ore and coke layers with fixed masses was inserted and settled under gravity. This procedure was repeated until the first few layers of ore had reached the predefined CZ which presents itself in Figure 2a with an abrupt change between layer and coke-only structure. Then, we performed the alternation of

CFD–DEM simulations to obtain particle velocity and porosity fields and data-assisted CFD to propagate the temperature field and obtain a new CZ. Figure 2b underlines that the latter had undergone a significant transformation after the observation period. After each data-assisted episode, an update of the CZ made itself visible the first few seconds of the following CFD–DEM simulations. As shown in **Figure 3**, the slipping down of coke into regions previously occupied by ore caused a rather irregular dynamics in terms of the total particle number. However, once this property had stabilized again and followed an almost periodic cycle of decrease and recharging as a sawtooth wave, we could start to sample flow fields for the following data-assisted run. The velocity fields for the first and the fourth one

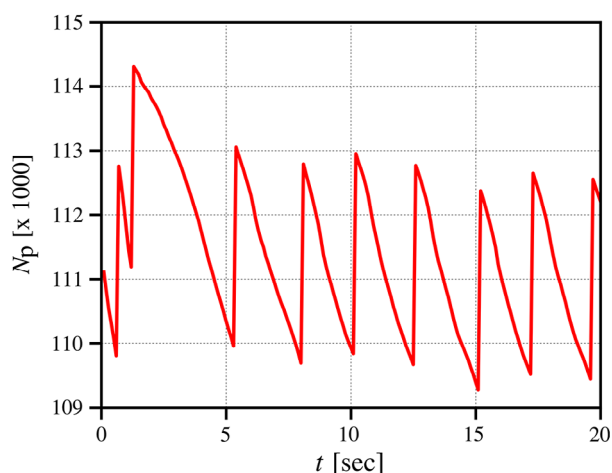


Figure 3. Number of particles in a CFD–DEM BF simulation over time. After an initial equilibration phase caused by an update of the CZ, a relatively regular pattern of material decrease due to melting and gasification in the CZ and the raceways, respectively, followed by recharging once the particle level had come below a certain threshold, developed. Only after a “safety period” of at least 20 s, flow fields were sampled for the use in data-assisted simulations.

are shown in **Figure 4**. Even though the paths along which the grains traveled hardly changed at all, the dynamic nature of the CZ affected their velocity evolution, their residence time, and of course the location where ore grains would melt. Because we binned particle velocities on the CFD mesh (with cell sizes somewhat larger than parcels) and subsequently averaged them over a few layer passage times, the resulting fields were much smoother than what one would expect from typical granular stick–slip motion.

The importance of repeated updates of the particle dynamics becomes visible in the temperature fields in **Figure 5**. A pronounced change in the temperature field is clearly connected to a change in shape and location of the CZ which turned from an inverted V toward a weak W. This behavior indicates that our simulation actually corresponded to a “wall-working furnace”.^[45] The sequence of Figure 5a–d demonstrates that this transformation was a gradual process taking place over many hours and would not have been accessible from short-term investigations.

From the mean particle temperature over time $\bar{T}_p(t)$ shown in **Figure 6**, it can be deduced that our simulations had converged to a satisfying degree. Not only did $\bar{T}_p(t)$ fluctuate around a fixed value during the last two data-assisted runs (the oscillations were caused by removal and recharging of material) but also did the CZ update between the third and fourth episode cause hardly any changes in the temperatures anymore. This observation is further backed up by line plots of particle temperatures shown in **Figure 7**. Although a massive adaption took place during the first few hours, the system had reached its steady-state configuration after about 10 h after which no significant changes could be observed anymore. Hence, our simulations had covered a sufficient process duration to find the thermal equilibrium state of the BF.

All calculations were carried out on 8 cores, with wall times of about 18.3 and 28.4 h for each CFD–DEM and data-assisted CFD run corresponding to 20 s and 5 h real time, respectively. Hence, it took about eight days for our iterated procedure starting from the initial configuration to reach the final one shown in Figure 1.

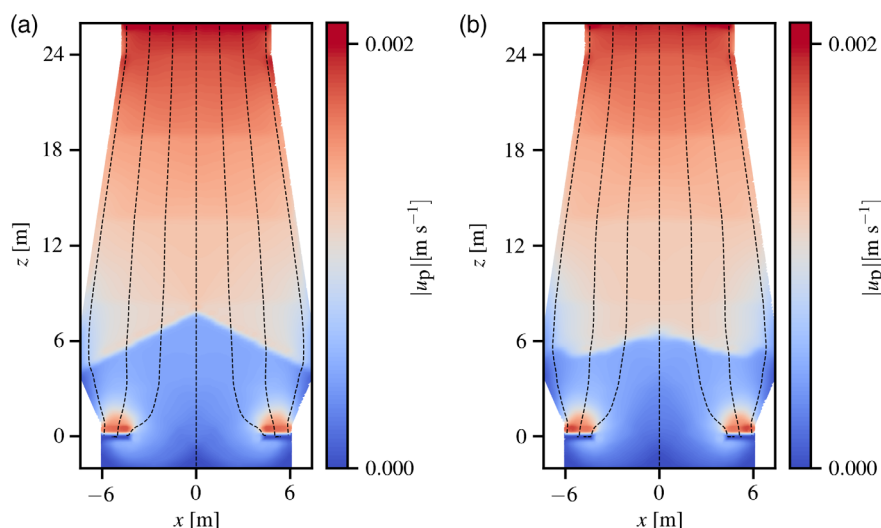


Figure 4. Particle velocity field for the a) first and b) fourth data-assisted episode. The change of the CZ influenced where grains had larger velocities because voids were created below due to melting, and where they had lower ones. Particle stream lines indicated by the dashed curves are less affected.

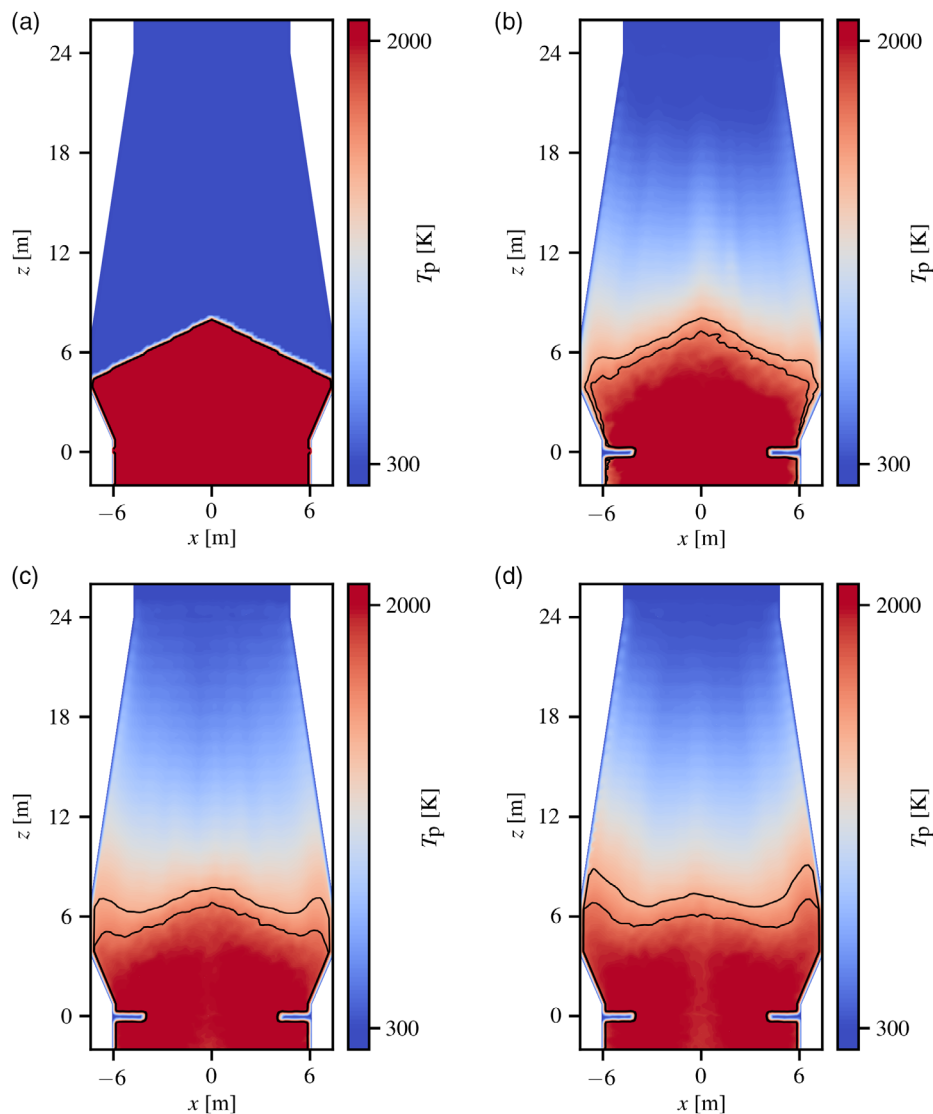


Figure 5. Particle temperature field in the mid-plane at different times. a) Initially, we guessed a shape of CZ with high temperatures below and lower ones above it. After b) 5 h, the sharp transition had already started softening and a finite-width CZ indicated by the black lines had developed. Over the course of c) 10 h and d) 20 h, its shape changed from an inverted V toward a weak W.

One could save some time in the data-generating CFD–DEM episodes because Figure 3 indicates that they relaxed toward their new steady state within a few seconds process time, so that one might reduce $\tau_{\text{CFD-DEM}}$ from 20 s to e.g., 15 s. However, the main computational costs stemmed from the data-assisted CFD calculations (more specifically from the solution of the Navier–Stokes equations and the evaluation of the particle–fluid interaction accounting for $\approx 80\%$ and 10% of the total data-assisted runtime). Unless a criterion to detect the approach to the final thermal steady state earlier than by monitoring the mean particle temperature over two consecutive episodes can be devised, the most straightforward further reduction of wall times may be achieved with increasing the computational resources and performing the calculations on more cores. However, we stress that communication overheads will limit the possible gains, e.g., because large grain displacements inherent in

data-assisted CFD with tracers cause very frequent transfers of particles between processors, which happens even more often with increasing the number of processors. Hence, we assume that currently, wall times on the order of several days need to be accepted to study the behavior of large-scale BFs over process-relevant durations, which is still far less than standard CFD–DEM could provide.

5. Conclusion, Outlook, and Challenges

In this work, we have presented an extremely fast, data-assisted simulation strategy for dense gas–solid flows as found, e.g., in shaft or BFs. Our approach uses detailed CFD–DEM information, but outperforms this method with speed-ups of several orders of magnitude. In the presented example, our data-assisted

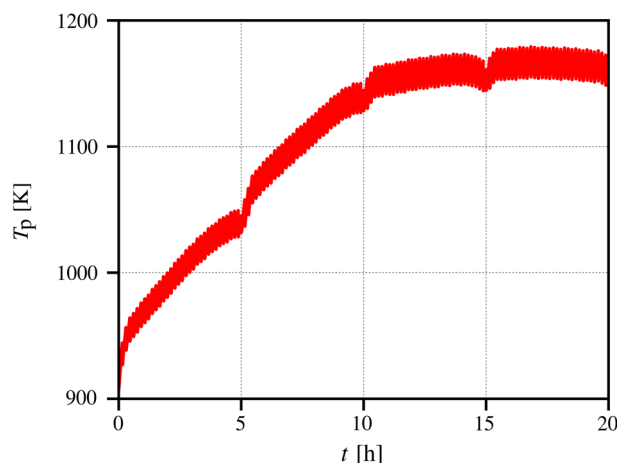


Figure 6. Mean particle temperature over time. A fast, initial increase was followed by a slow approach toward the steady-state value. Changes in the CZ after 5 h, 10 h, and 15 h gave rise to slight jumps. After 20 h, the averaged particle temperature was approximately converged both within a single data-assisted episode and also between two consecutive ones.

calculations ran about a factor of 600 faster than corresponding CFD–DEM simulations on the same hardware. For 1 s of process duration, the former took ≈ 5.7 s of CPU time while the latter required 3300 s (both on 8 cores). As they rely on previously obtained, detailed data, we have in particular shown the importance to update them during long-term studies to account for backcoupling of slow processes such as heat transfer on the underlying dynamics. In this work, we paid specific attention to the location and shape of the CZ which of course depends on the particles' temperatures but in turn affects their dynamics.

It goes without saying that the presented model has been strongly simplified in several regards for the sake of a clear, straightforward explanation of the novel algorithmic strategy. However, none of these simplifications is beyond the scope of our method. To introduce our computational strategy, we have chosen a slot model which resulted in a simpler setup and lower particle and cell numbers, but did not reflect the full physics of a 3D furnace. Going to an actual 3D geometry poses no difficulty for data-assisted CFD with tracers in addition to somewhat larger

computational costs due to an increase in grain and cell number. However, this effect can easily be outbalanced using more than only 8 cores as done in the present work for the larger domain, which may be expected to work much more efficiently than increasing their number at constant system size as discussed in the previous section.

Furthermore, there are several physical and chemical phenomena which call for inclusion in future work. Clearly, calculating temperature fields without a proper treatment of radiative heat transfer as well as homo- and heterogeneous chemical reactions has mainly conceptual value. Adding species transport to the hierarchy of fluid equations of motion will have an impact on runtimes because fast reactions within the fluid phase typically reduce time step size and/or increase the number of iterations for the numerical solution to converge. Ore reduction, in contrast, takes place rather slowly so that the corresponding equations need not be solved in every step, but e.g., only every 100th.

Once chemical processes will be accounted for, it will also be necessary to picture the raceway regions, where some of the most important reactions take place more accurately. Instead of prescribing a static shape as done in this work, it should be calculated during the CFD–DEM episodes. In this regard, one has to find a balance between large coarse-graining factors to limit the total grain number and small ones to allow for a proper resolution of the raceways. For such scenarios, embedded simulations as introduced by Queteschiner et al.^[46,47] could provide a way out of this predicament. In subdomains of particular interest, a higher resolution both in terms of mesh and parcel size is chosen and coupled with the less resolved surroundings by exchanging forcing terms. The same technique could also be used to picture permeable coke windows in the CZ, which can hardly be resolved in massively coarse-grained calculations.

Finally, one may include trickling of molten iron and slag down through the coke bed before they reach the pool of liquids in the BF hearth. Although a numerically cheap method to simulate drainage under stratified flow in a CFD(–DEM) framework is available,^[33] detailed studies on the droplet dynamics need to be carried out from which a simplified model can be derived that does not add too much computational costs to our data-assisted method and that does not rely on particle-level packing information and contact structure which are not available in our calculations.

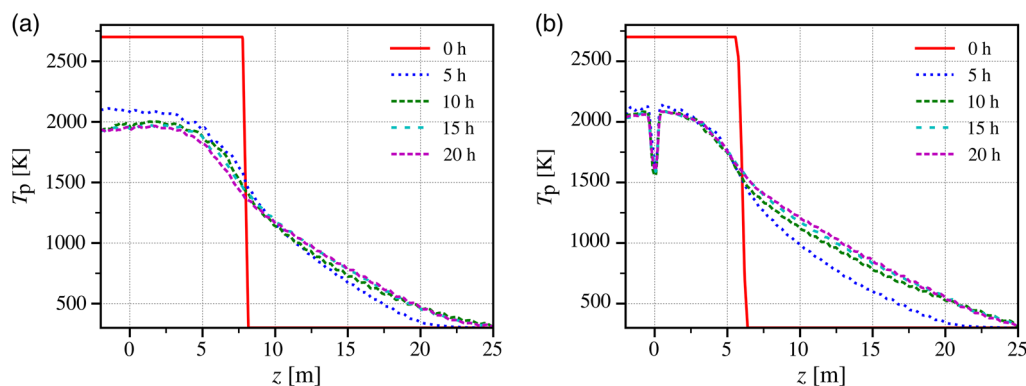


Figure 7. Particle temperature over height in the center of the BF with a) $x = 0$ m and b) close to the side with $x = 4.5$ m. After 10 h process time, only minor changes in the temperature field took place anymore.

Although the aforementioned phenomena can in principle all be included in our approach with moderate additional costs so that process-relevant durations can still be covered, we want to point out a much more challenging issue, too. In practice, moving bed reactors are infamous for flow irregularities such as (spontaneous) channel formation with accompanying poor gas–solid contact or hanging and subsequent collapse of the bed. Clearly, such atypical behavior cannot be encountered in our present simulations built upon a single particle velocity and porosity field at a time. It will take in-depth investigations to explore the physical origins of these phenomena and to possibly identify order parameters indicating imminent process irregularities so that data-assisted calculations could be stopped on demand and detailed CFD–DEM simulations used instead to picture channeling or hanging.

Even though there are several open tasks, the presented strategy of combined CFD–DEM and fast, data-assisted CFD constitutes a significant step toward virtual experiments on real BFs with sufficient flexibility to include various physical and chemical phenomena relevant for industrial purposes.

Acknowledgements

This work was partly funded by the Linz Institute of Technology (LIT), Johannes Kepler University, Linz. Furthermore, the authors gratefully acknowledge the funding support of K1-MET GmbH, metallurgical competence center. The research program of the K1-MET competence center is supported by COMET (Competence Center for Excellent Technologies), the Austrian program for competence centers. COMET is funded by the Federal Ministry for Transport, Innovation and Technology, the Federal Ministry for Digital and Economic Affairs, and the provinces of Upper Austria, Tyrol, and Styria. In addition to the public funding from COMET, this research project is partially financed by the industrial partners voestalpine AG and Primetals Technologies Austria GmbH.

Conflict of Interest

The authors declare no conflict of interest.

Keywords

blast furnaces, cohesive zone, data-assisted simulations, discrete element method, heat transfer

Received: March 12, 2020
Revised: April 29, 2020
Published online: May 29, 2020

- [1] K. L. Johnson, *Contact Mechanics*, Cambridge University Press, Cambridge, UK **1985**.
- [2] J.-I. Yagi, *ISIJ Int.* **1993**, 33, 619.
- [3] P. R. Austin, H. Nogami, J.-I. Yagi, *ISIJ Int.* **1997**, 37, 748.
- [4] J. A. de Castro, H. Nogami, J.-I. Yagi, *ISIJ Int.* **2002**, 42, 44.
- [5] H. Nogami, M. Chu, J.-I. Yagi, *Comput. Chem. Eng.* **2005**, 29, 2438.
- [6] J. A. de Castro, G. de Mattos Araújo, I. O. da Mota, Y. Sasaki, J.-I. Yagi, *J. Mater. Res. Technol.* **2013**, 2, 308.
- [7] S. Natsui, H. Takai, R. Nashimoto, T. Kikuchi, R. O. Suzuki, *Int. J. Heat Mass Transf.* **2015**, 91, 1176.
- [8] P. A. Cundall, O. D. L. Strack, *Géotechnique* **1979**, 29, 47.
- [9] Y. Tsuji, T. Kawaguchi, T. Tanaka, *Powder Technol.* **1993**, 77, 79.
- [10] N. G. Deen, M. Van Sint Annaland, M. A. Van der Hoef, J. A. M. Kuipers, *Chem. Eng. Sci.* **2007**, 62, 28.
- [11] C. Bierwisch, T. Kraft, H. Riedel, M. Moseler, *J. Mech. Phys. Solids* **2009**, 57, 10.
- [12] M. Sakai, S. Koshizuka, *Chem. Eng. Sci.* **2009**, 64, 533.
- [13] T. Mitra, H. Saxén, *IFAC-PapersOnLine* **2015**, 48, 183.
- [14] Z. Y. Zhou, H. P. Zhu, A. B. Yu, B. Wright, P. Zulli, *Comput. Chem. Eng.* **2008**, 32, 1760.
- [15] W. J. Yang, Z. Y. Zhou, A. B. Yu, *Chem. Eng. J.* **2015**, 278, 339.
- [16] S. Ueda, T. Kon, H. Kurosawa, S. Natsui, T. Ariyama, H. Nogami, *ISIJ Int.* **2015**, 55, 1232.
- [17] H. Nogami, H. Yamaoka, K. Takatani, *ISIJ Int.* **2004**, 44, 2150.
- [18] J. E. Hilton, P. W. Cleary, *Chem. Eng. Sci.* **2012**, 80, 306.
- [19] Z. Miao, Z. Zhou, A. B. Yu, Y. Shen, *Powder Technol.* **2017**, 314, 542.
- [20] E. R. Santana, G. Pozzetti, B. Peters, *Chem. Eng. Sci.* **2019**, 205, 46.
- [21] J. Cui, Q. Hou, Y. Shen, *Powder Technol.* **2020**, 362, 539.
- [22] Q. Hou, D. E., S. Kuang, Z. Li, A. B. Yu, *Powder Technol.* **2017**, 314, 557.
- [23] G. Cheng, J. Gan, D. Xu, A. Yu, *Powder Technol.* **2020**, 361, 326.
- [24] H. Wu, N. Gui, X. Yang, J. Tu, S. Jiang, *Chem. Eng. Sci.* **2020**, 211, 115309.
- [25] M. Vångö, S. Pirker, T. Lichtenegger, *Appl. Math. Model.* **2018**, 56, 501.
- [26] F. Bambauer, S. Wirtz, V. Scherer, H. Bartusch, *Powder Technol.* **2018**, 334, 53.
- [27] Q. Hou, D. Bluhm-Drenhaus, S. Kuang, A. Yu, *Fuel Process. Technol.* **2020**, 202, 106369.
- [28] X. Wen, O. T. Stein, G. L. Tufano, A. Kronenburg, A. Scholtissek, C. Hasse, *Fuel* **2019**, 255, 115772.
- [29] T. Bluhm-Drenhaus, E. Simsek, S. Wirtz, V. Scherer, *Chem. Eng. Sci.* **2010**, 65, 2821.
- [30] B. Krause, B. Liedmann, J. Wiese, S. Wirtz, V. Scherer, *Chem. Eng. Sci.* **2015**, 134, 834.
- [31] B. Krause, B. Liedmann, J. Wiese, P. Bucher, S. Wirtz, H. Piringer, V. Scherer, *Int. J. Therm. Sci.* **2017**, 117, 121.
- [32] X. Bednarek, S. Martin, A. Ndiaye, V. Peres, O. Bonnefoy, *Chem. Eng. Sci.*, **2019**, 197, 223.
- [33] M. Vångö, C. Feilmayr, S. Pirker, T. Lichtenegger, *Appl. Math. Model.* **2019**, 73, 210.
- [34] T. Lichtenegger, *Powder Technol.* **2020**, 362, 474.
- [35] T. Lichtenegger, E. A. J. F. Peters, J. A. M. Kuipers, S. Pirker, *Chem. Eng. Sci.* **2017**, 172, 310.
- [36] W. Ranz, W. Marshall, *Chem. Eng. Prog.* **1952**, 48, 141.
- [37] S. Slaby, D. Andahazy, F. Winter, C. Feilmayr, T. Bürgler, *ISIJ Int.* **2006**, 46, 1006.
- [38] S. Torquato, F. H. Stillinger, *Rev. Mod. Phys.* **2010**, 82, 2633.
- [39] T. B. Anderson, R. Jackson, *Ind. Eng. Chem. Fundam.* **1967**, 6, 527.
- [40] M. Syamlal, D. Gidaspow, *AIChE J.* **1985**, 31, 127.
- [41] J. K. Carson, S. J. Lovatt, D. J. Tanner, A. C. Cleveland, *Int. J. Heat Mass Transf.* **2005**, 48, 2150.
- [42] C. Kloss, C. Goniva, A. Hager, S. Amberger, S. Pirker, *Prog. Comput. Fluid Dyn.* **2012**, 12, 140.
- [43] C. Goniva, C. Kloss, N. G. Deen, J. A. M. Kuipers, S. Pirker, *Particuology* **2012**, 10, 582.
- [44] Z. Zhang, J. Meng, L. Guo, Z. Guo, *Metall. Mater. Trans.* **2016**, 47, 467.
- [45] M. Geerdes, R. Chaigneau, I. Kurunov, *Modern Blast Furnace Ironmaking: An Introduction*, IOS Press, Fairfax, VA **2015**.
- [46] D. Queteschiner, T. Lichtenegger, S. Schneiderbauer, S. Pirker, *Part. Sci. Technol.* **2018**, 36, 517.
- [47] D. Queteschiner, T. Lichtenegger, S. Pirker, S. Schneiderbauer, *Powder Technol.* **2018**, 338, 614.